A reinvestigation of $Na_2Fe_2(C_2O_4)_3 \cdot 2H_2O$: an iron-based positive electrode for secondary batteries

Wenjiao Yao,[†] Moulay-Tahar Sougrati,[§,‡] Khang Hoang,[¶] Jianing Hui,[†] Philip Lightfoot,[†,*] A. Robert Armstrong[†,‡*]

[†] School of Chemistry, University of St Andrews, St Andrews, Fife KY16 9ST, United Kingdom

[§] Université de Montpellier, 2 Place Eugène Bataillon - CC 1502, 34095 Montpellier CEDEX 5, France

[¶] Department of Physics, North Dakota State University, Fargo, North Dakota 58108, United States

[‡] ALISTORE-ERI, 80039, Amiens Cedex, France

ABSTRACT: We have reinvestigated the polyanionic compound $Na_2Fe_2(C_2O_4)_3 \cdot 2H_2O$, previously reported to be electrochemically inactive in lithium-ion batteries (LIBs), as a positive electrode for sodium-ion batteries (NIBs). The present study demonstrates that it is capable of delivering a reversible capacity close to its theoretical value (117 $mAhg^{-1}$) with three redox plateaus at 2.9, 3.3 and 3.6 V vs. Na/Na^+ in the potential range 1.7–4.2 V. The obtained energy density of 326 $WhKg^{-1}$ is among the highest of all reported polyanionic cathodes in NIBs. The origin of the electrochemical activity can be traced back to the electronic structure of the compound and the low migration energy barrier of the alkali ion observed in first-principles density-functional theory calculations.

I. INTRODUCTION

The demand for large-scale storage of electricity generated from renewable sources such as wind and solar is attracting ever-increasing attention. Among the alternatives are those which employ batteries; despite the overwhelming role of lithium-ion batteries (LIBs) in portable devices, they are unlikely to dominate the grid storage sector due to the low abundance and high cost of lithium sources. Sodium-ion batteries (NIBs) provide an attractive alternative thanks to the high abundance, wide and even geographic distribution, and resemblance to lithium (second lightest alkali element in periodic table).[1] Increasing efforts have been devoted to build efficient NIBs with optimization of energy density, high safety as well as long-term durability.[2–3] In terms of transition metal, iron is the most desirable redox center due to its low cost, low toxicity and electrochemical activity. As a result, several Fe-based cathodes have been investigated. The simple layered oxide phases (counterparts to commercial cathodes in LIBs), including O3-type $NaFeO_2$[4] and P2-type $Na(Fe_{0.5}Mn_{0.5})O_2$,[5–6] suffer from limited cycling stability. In this sense, polyanion-based compounds may provide higher and tunable operating potentials due to the inductive effect, as well as robust and therefore stable frameworks due to strong covalent bonds. Examples are Na_2FePO_4F,[7–8] $NaFePO_4$,[9] $Na_2FeP_2O_7$,[10] $Na_4Fe_3(PO_4)_2(P_2O_7)$,[11] $NaFe_3(HPO_3)_9$,[12] $NaFe(PO_3)_3$,[13] $Na_2Fe_2(SO_4)_3$,[14] $NaFe(SO_4)_2$,[15] and $Na_2FeC_2O_4F_2$.[16]

As demonstrated by our previous work,[16] transition metals in oxalates display redox potentials lower than those of sulfates but comparable to those of phosphates, which reflects the electronegativity of $(SO_4)^{2-} > (C_2O_4)^{2-} > (PO_4)^{3-}$.

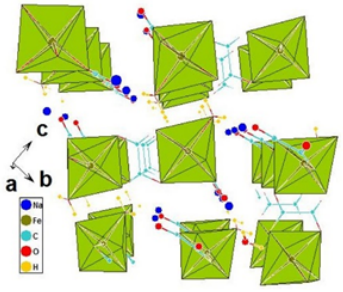

Figure 1. Structure of $Na_2Fe_2(C_2O_4)_3 \cdot 2H_2O$ viewed along the *a*-axis. FeO_6 octahedra are shown in green.

We observed that among the oxalates that have been characterized electrochemically, all are reported to be active except $Na_2Fe_2(C_2O_4)_3 \cdot 2H_2O$.[17–19] This compound was originally reported as a magnetic material due to the oxalate-provided spin exchange pathway for the 3d electrons of iron.[20–21] In 2015, Tarascon's group tested the electrochemical performance in LIBs, and reported negligible electrochemical activity. In detail, an experimental capacity of 35 $mAhg^{-1}$ was obtained at an average potential of 3.3 V vs. Li/Li^+ between 2.0 and 4.2 V at a rate of C/10. In addition, Mössbauer spectroscopy showed essentially no oxidized iron in the charged state. As reported previously, the structure features one dimensional chains along the *a*-axis as shown in **Figure 1**, which provide a relatively loosely-bonded environment and an unrestricted migration path for Na^+. Therefore we reinvestigated the electrochemical properties of this material in sodium cells. By contrast with the previously published results from lithium cells, it displayed a capacity approaching the theoretical value (117 $mAhg^{-1}$), with high potential redox processes

at 2.9, 3.3, and 3.6 V, and excellent cyclability when used as positive electrode in NIBs. The Mössbauer spectra clearly showed oxidized iron, which is also consistent with the features of the electronic structure of the compound observed in first-principles calculations.

II. EXPERIMENTS

2.1 Synthesis and characterization

Single crystals of the title compound were synthesized by a hydrothermal method. Typically, as-obtained $FeCl_2 \cdot 2H_2O$, $H_2C_2O_4 \cdot 2H_2O$, Na_2CO_3 were mixed in a teflon-lined autoclave in the ratio of 2:3:4 (1 for 5 mmol), with 2 mL H_2O added as solvent. The autoclave was heated at 160°C for three days and then cooled in air. The resulting products were repeatedly washed with distilled water and acetone and dried at 60°C. Powder X-ray diffraction (XRD) patterns were recorded on a Stoe STADI/P diffractometer operating in either transmission mode or Debye-Scherrer mode with Fe $K\alpha_1$ radiation (λ = 1.936 Å) in the 2θ range 10°–90°. Scanning electron microscopy (SEM) images of prepared samples were taken on a JEOL JSM-6700F equipped with a field emission gun (FEG) electron source. Secondary electron images were recorded with a tungsten filament electron source using an accelerating voltage of 5 kV for the hand ground pristine sample, and 15 kV for ball-milled cathode samples. A retractable backscattered electron detector was applied for atomic number contrast imaging.

2.2 Electrochemistry

The material was mixed with Ketjenblack carbon in the weight ratio of 2:1 for 30 minutes using a Fritsch Pulverisette 8 mill. Subsequently the powder was ground with binder (poltetrafluoroethylene, PTFE, 10% by wt.) until homogeneous and pressed into pellets containing 6–8 mg active material. These were fabricated in coin cells (CR2325, NRC Canada) in an Ar-filled glove box with Na metal as anode, 1 M $NaClO_4$ in propylene carbonate with 3% fluoroethylene carbonate as electrolyte.

Half cells were then tested by galvanostatic cycling over various potential windows at rates of 5, 10 or 20 mAg^{-1} using a Biologic Macpile II system. Cells for *ex situ* characterization in the charged or discharged state used larger amounts of active material and Kynar Flex 2801 (a copolymer based on PVDF) as binder. The electrode was then removed in an Ar-filled glove box, washed with dry dimethyl carbonate (DMC) and dry THF and dried by slow evaporation.

2.3 Mössbauer spectra

Room temperature Mössbauer spectra were recorded on absorbers prepared under argon (coffee-bags). Each absorber contains 30–40 mg/cm² active material recovered by washing with dimethyl carbonate (DMC). The spectrometer is operating in the constant acceleration transmission geometry. The γ-ray source (^{57}Co/Rd, 850 MBq) is maintained at room temperature. The isomer shift scale is calibrated using pure α-Fe standard. The obtained data are fitted using least-squares method and a combination of Lorentzian lines with MOSFIT program.

2.4 First-principles calculations

The calculations were based on density-functional theory within the generalized-gradient approximation[22] and the projector-augmented wave method,[23] as implemented in the Vienna *Ab Initio* Simulation Package (VASP).[24] We applied the on-site Hubbard correction[25] with the effective U value of 4.0 eV on the Fe 3d states; the van der Waals correction was included using Grimme's method.[26] For the total-energy calculations of $Na_2Fe_2(C_2O_4)_3 \cdot 2H_2O$, we used a Γ-centered 6×2×5 **k**-point mesh; a denser, 7×3×6, **k**-point mesh is used in calculations to obtain electronic densities of states. The migration of Na (and Li) in the material was studied using 2×1×2 (224-atom) supercells and the climbing-image nudged elastic band (NEB) method.[27] In all calculations, the energy cutoff was set at 500 eV and spin polarization was included.

III. RESULTS AND DISCUSSION

Crystalline samples were prepared by mild hydrothermal synthesis. The orange crystallites were easily separated from colorless byproducts via washing with distilled water. Both single crystal and powder XRD were carried out on the dried sample. The cell parameters obtained from sin gle crystal XRD agreed well with reported values (*Supporting Information*, Table S1).[20–21] Rietveld refinement of the powder XRD pattern of a hand-ground sample (**Figure 2(a)**) revealed that the sample is isostructural with that determined from low temperature (–100°C) single crystal XRD, with small expansions along all crystallo

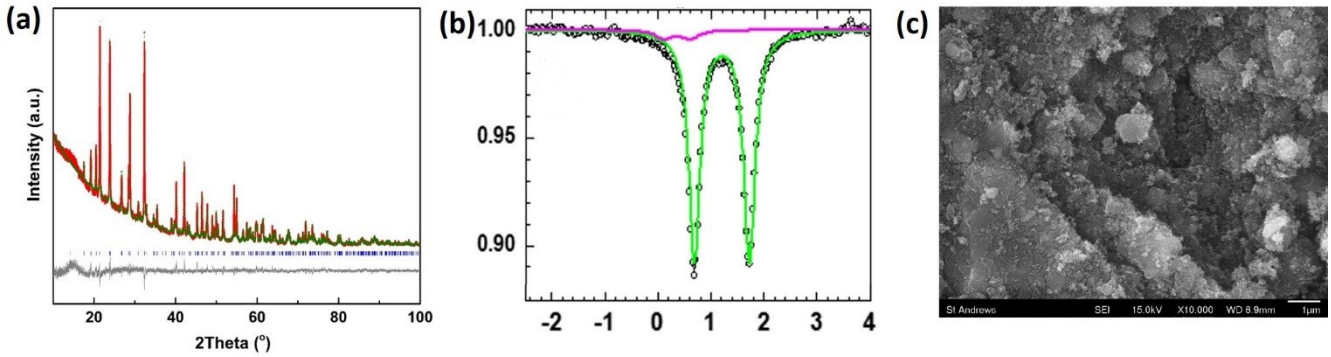

Figure 2. Characterization of $Na_2Fe_2(C_2O_4)_3 \cdot 2H_2O$. (a) Rietveld refinement of room temperature powder XRD on a pristine sample. $P2_1/c$ space group, a = 5.9117(1) Å, b = 15.7838(2) Å, c = 7.0832(1) Å , β = 100.338(4)°, wR_p=0.0556, R_p=0.043, χ^2=1.58. (b) Room temperature Mössbauer spectrum and (c) SEM image of ball-milled sample with conductive carbon.

graphic directions. The refinement also confirmed that the sample was of high purity.

The hydrothermally obtained pristine material was ball milled with Ketjenblack carbon to improve the electronic conductivity of the pure sample and to reduce the particle size. Figure 2(b) displays the Mössbauer spectrum of the aforementioned composite. It is shown that the iron is mostly (95%) present in a unique environment with an isomer shift of 1.20 mm/s, a quadrupole splitting (Δ) of 1.04 mm/s and a linewidth (Γ) of 0.26 mm/s, suggesting a high spin Fe^{2+} in octahedral coordination (Table S2). The slight asymmetry of the spectrum is due to a minor Fe^{3+} component (δ = 0.35 mm/s, Γ= 0.48 mm/s).[19] The trace amount of impurity was probably due to surface oxidation during ball-milling or a slight loss of sodium (non-stoichiometry). The morphology of the ball-milled mixture was checked by SEM, as shown in Figure 2(c). This verified that the target compound was well dispersed in Ketjenblack carbon, with an average size of 1 μm. The powder XRD pattern of the ball-milled composite showed significant peak broadening compared with the hand ground material (Figure S1), confirming that ball-milling diminished crystallite size effectively.

Figure 3(a) displays galvanostatic voltage profiles in the voltage window of 1.7–4.2 V at rates of C/20, C/10 and C/5. Notably, a capacity of 116.6 $mAhg^{-1}$ was obtained when applying a current of 5 mAg^{-1}, which is almost equal to the theoretical capacity (117 $mAhg^{-1}$) and corresponds to an energy density of 326 $Whkg^{-1}$. Meanwhile, 84% and 76% of theoretical capacity were obtained for the rates of C/10 and C/5, respectively. Figure 3(b) shows the capacity retention for the first 30 cycles at a rate of 10 mAg^{-1}. It can be seen that the capacity increases slightly over the first few cycles, before stabilizing. The increase of capacity is probably a result of an electrochemical grinding effect resulting in improved electronic conductivity in the electrode. This is supported by a progressive reduction in the cell polarization as a function of cycle number as shown by load curves (Figure S2). Similar phenomena have been observed in several other electrode materials.[28–29] After 25 cycles, the discharge capacity remained at 100 $mAhg^{-1}$, corresponding to exchange of 1.7 Na^+ ions per formula unit, with a Coulombic efficiency approaching 100%. The initial charge-discharge curve is rather smooth without obvious plateaus. After 25 cycles, well-defined processes become apparent, clearly displaying three plateaus at 2.9, 3.3 and 3.6 V, as illustrated in Figure 3(c). Such a phenomenon is quite common in battery materials, where although there may only be a single cation site several plateaus are observed. This can arise from a variety of reasons such as vacancy or charge ordering. Examples include $LiMn_2O_4$ and $LiCoPO_4$.[30-31] In this case it appears that the plateaus at 3.3 and 3.6V have this origin, being approximately half the length of that at 2.9V. Unfortunately the low crystallinity of this material precludes detailed structural analysis.

In order to understand the redox mechanism of $Na_2Fe_2(C_2O_4)_3 \cdot 2H_2O$, recovered electrodes charged to 4.2V and discharged to 2.0 V were subjected to Mössbauer spectroscopy. The spectrum from the charged sample is depicted in Figure 3(d). It is shown that the charged material contains predominantly oxidized Fe^{3+} (red), 26% of unreacted Fe^{2+} corresponding to the pristine material

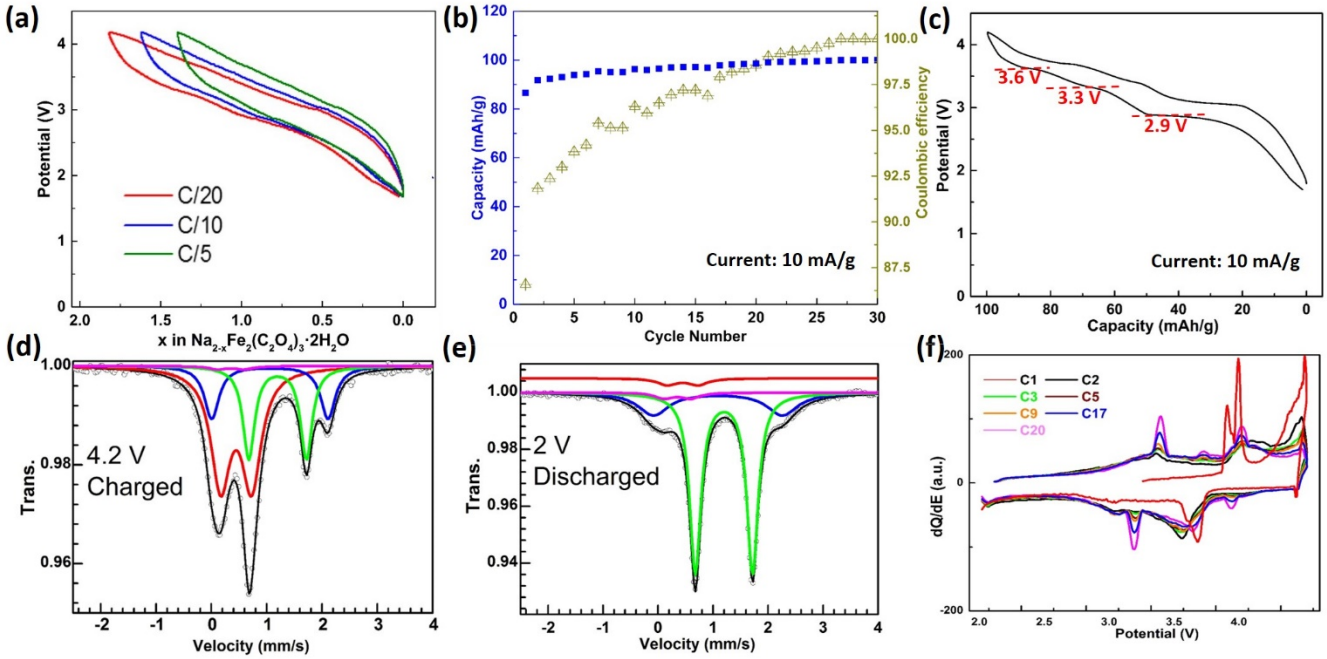

Figure 3. Half-cell performance of $Na_2Fe_2(C_2O_4)_3 \cdot 2H_2O$ in NIB. (a) Galvanostatic voltage profiles in the voltage range of 1.7–4.2 V at rates of C/20, C/10 and C/5. (b) Capacity retention and Coulombic efficiency at a cycling rate of 10 mAg^{-1}; (c) Galvanostatic voltage profiles at the 25th cycle. (d–e) Mössbauer spectra of 4.2 V-charged and 2.0 V-discharged cathode. Green, blue, red, and pink stands for Fe^{2+} in original and new site, and Fe^{3+} of oxidized and in impurity, respectively. Red line in (e) is shifted to make it clearer. (f) Differential capacity plots of the initial 20 cycles.

(green) and a small amount of a new Fe^{2+} environment (blue). The unreacted Fe^{2+} (green) is readily understood in terms of the difference between theoretical capacity and the value obtained at a rate of 10 mAg^{-1}. The new Fe^{2+} environment may arise as a result of altering the Fe^{2+} environment during sodium extraction. Figure 3(e) shows the spectrum after charge and subsequent discharge to 2.0 V, revealing that most of the oxidized Fe^{3+} has been reduced to its initial state. The initial impurity spectrum remained unchanged in both charged and discharged materials (Table S2).

Detailed examination of the differential galvanostatic profile, as shown in Figure 3(f) reveals a progressive evolution and sharpening of the oxidation/reduction peaks with a concomitant reduction in cell polarization. The rather indistinct features of the first few cycles resolve into discharge processes at 2.9 V, 3.3 V, and 3.6 V, with a cell polarization of around 0.1 V; all peaks are stabilized after 20 cycles. It is clear that the cell went through a continuous slow reaction over initial 20 cycles. Such a progressive change could be caused either by an electrochemically-driven phase transition (structural rearrangements) as observed in $LiMnO_2$,[32] Li_2FeSiO_4,[33–34] $Li_2FeP_2O_7$,[35–36] and $Na_2Fe_2(SO_4)_3$,[37] or be the result of electrochemical grinding.

In order to test these two possibilities, *ex situ* powder XRD and SEM were performed on the stabilized charged and discharged cathodes. Cells were subjected to 20 cycles in the potential window of 1.7–4.2 V at a rate of 10 mAg^{-1}, followed by charge/discharge at a current of 5mAg^{-1}, in order to allow complete desodiation/sodiation.

Figure 4(a) shows the PXRD pattern of the charged sample compared with that of the pristine sample. The obvious differences are reduced peak intensity at 17.54°, 30.87° and 31.45°, as highlighted by green shading. The blue lines correspond to a calculated PXRD pattern for "$Fe_2(C_2O_4)_3 \cdot 2H_2O$" derived from removal of the Na-site from the original $Na_2Fe_2(C_2O_4)_3 \cdot 2H_2O$ structure. It is clear that the change of experimental PXRD corresponds to the removal of a significant proportion of the Na in the structure without significant framework rearrangement. Rietveld refinement was also conducted on the charged sample (Figure S3). While the detailed structure could not be determined as a consequence of the low crystallinity induced by ballmilling, a satisfactory fit was obtained, revealing a notable lattice contraction. SEM images, both secondary electron image (SEI) and back scattered electron image (BSE), are displayed in Figures 4(b–c). BSE gives a clearer overview of the dispersed title compound in amorphous carbon than the SEI. The PXRD pattern of the discharged sample can be readily refined by the Rietveld method using the original structural model, as displayed in Figure 4(d). This is consistent with the retention of two water molecules in the structure. Since the water has an integral bridging role in the structure, the excellent cycling stability shown in Figure 3(b) provides further circumstantial evidence that the water is retained on cycling. Corresponding SEM images are shown in Figure 4(e–f). These *ex situ* powder XRD results eliminate the possibility of an electrochemically-driven phase transition.

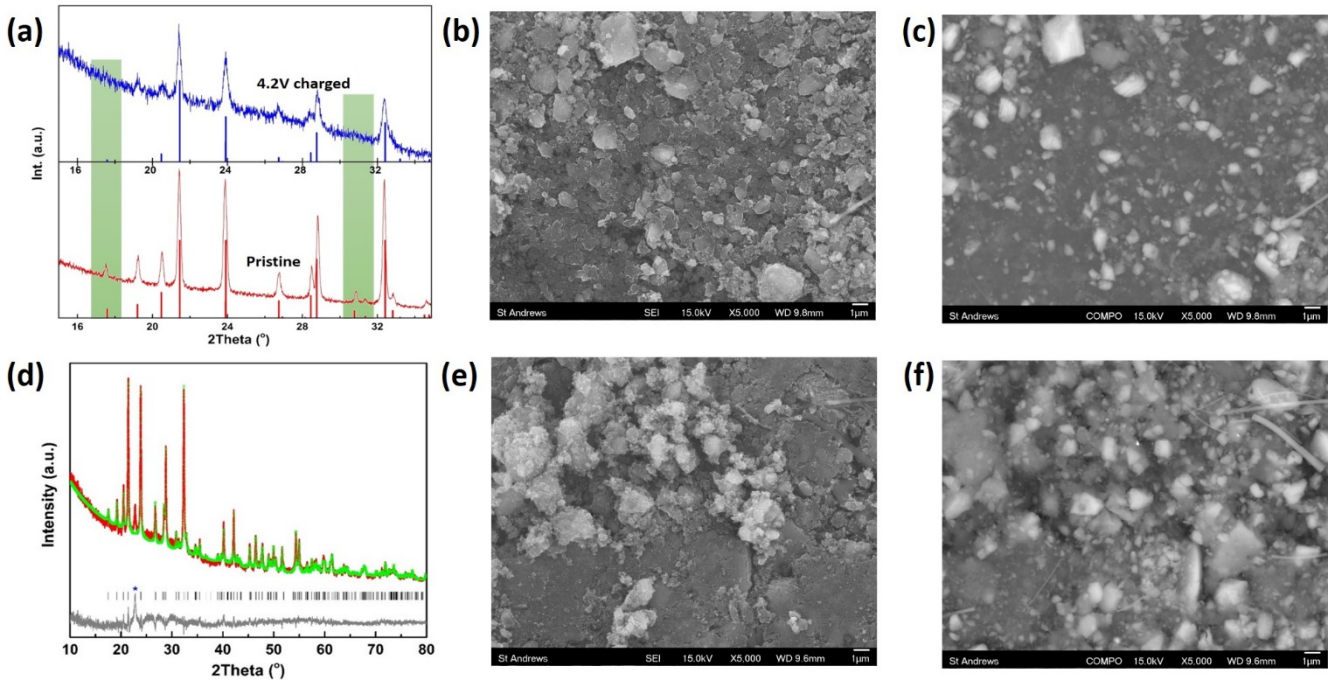

Figure 4. Characterization of after cycling in the charged and discharged state. (a) PXRD, (b) Secondary electron image (SEI), (c) Back scattered electron image (BSE) for charged cathode; (d) Rietveld refinement of PXRD on discharged material. $P2_1/c$ space group, a = 5.9114(2) Å, b = 15.7857(6) Å, c = 7.0843(3) Å, β = 100.328(3)°, wRp = 0.0628, Rp = 0.049, χ^2 = 2.057. (e) SEI, (f) BSE for discharged cathode.

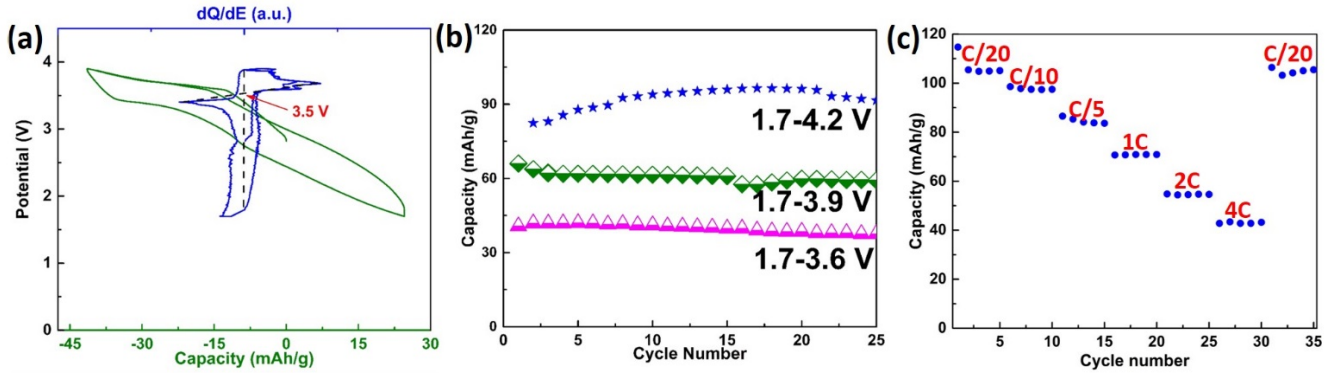

Figure 5. Half-cell performance of $Na_2Fe_2(C_2O_4)_3 \cdot 2H_2O$ in NIB in various voltage windows. (a) Galvanostatic and differential galvanostatic voltage profiles in the window of 1.7–3.9 V; (b) Capacity retention for different voltage windows; (c) Rate capability of $Na_2Fe_2(C_2O_4)_3 \cdot 2H_2O$ at various current densities in the window of 1.7-4.2 V.

Cells were also charged to different cut-off voltages of 3.6 V and 3.9 V. As shown in **Figure 5**(a–b), this delivered a stable capacity of 60 $mAhg^{-1}$ up to 3.9 V and 40 $mAhg^{-1}$ with an upper voltage limit of 3.6 V.

In order to further understand the origin of the electrochemical activity in $Na_2Fe_2(C_2O_4)_3 \cdot 2H_2O$, we carried out first-principles calculations for both the title compound and the hypothetical end-compound $Fe_2(C_2O_4)_3 \cdot 2H_2O$ where all Na are removed from the unit cell. We find that both compounds are stable after structural optimization. The calculated lattice parameters are a = 5.97 Å, b = 15.41 Å, c = 7.03 Å, and β = 99.08°, in good agreement with the experimental values. The optimized structure of $Fe_2(C_2O_4)_3 \cdot 2H_2O$ still possesses the monoclinic space group $P2_1/c$ with the lattice parameters a = 5.92 Å, b = 15.72 Å, c = 6.59 Å, and β = 107.29°. The results are consistent with the XRD experiments discussed above showing that the structure does not significantly change after Na removal. We find that iron in the title compound is stable as high-spin Fe^{2+} (with a calculated magnetic moment of 3.77 μ_B) whereas in the desodiated one it is high-spin Fe^{3+} (4.29 μ_B), in agreement with the Mössbauer isomer shift. In both compounds, the ferromagnetic (FM) and antiferromagnetic (AF) spin configurations are almost degenerate in energy. More specifically, the AF configuration in $Na_2Fe_2(C_2O_4)_3 \cdot 2H_2O$ is lower in energy than the FM one by 7 meV per formula unit (f.u.), whereas in $Fe_2(C_2O_4)_3 \cdot 2H_2O$, AF is lower than FM by 32 meV/f.u.

Figure 6 shows the electronic density of states of $Na_2Fe_2(C_2O_4)_3 \cdot 2H_2O$ and $Fe_2(C_2O_4)_3 \cdot 2H_2O$ in the AF spin configuration. The sodiated and desodiated compounds have calculated band gaps of 2.34 eV and 2.10 eV, respectively. We focus on the nature of the electronic structure near the band edges as it provides information about the intrinsic extraction and (re-)insertion mechanism.[38] It can be seen from the figure that the top of the valence band of $Na_2Fe_2(C_2O_4)_3 \cdot 2H_2O$ is predominantly composed of the highly localized Fe 3d states, whereas the bottom of the conduction band is predominantly C and O 2p states. Since Na extraction from the NIB cathode involves removing electrons from the highest occupied states, the electronic structure indicates that this process occurs through oxidation at the Fe^{2+} sites. The valence-band top of $Fe_2(C_2O_4)_3 \cdot 2H_2O$ is, on the other hand, predominantly C and O 2p states, whereas the conduction-band bottom is predominantly the unoccupied Fe 3d states. As Na (re-)insertion involves adding electrons to the lowest unoccupied states, this process occurs through reduction at the Fe^{3+} sites. These results are thus consistent with the observed Fe^{3+}/Fe^{2+} reversible redox reactions. The average redox potential is calculated to be 3.89 V vs Na between $Na_2Fe_2(C_2O_4)_3 \cdot 2H_2O$ and $Fe_2(C_2O_4)_3 \cdot 2H_2O$, well within the voltage range shown in Fig. 3(a). We note that the Li analog of $Na_2Fe_2(C_2O_4)_3 \cdot 2H_2O$ has a similar electronic structure, suggesting that the material can also be electrochemically active; the calculated redox potential between $Li_2Fe_2(C_2O_4)_3 \cdot 2H_2O$ and $Fe_2(C_2O_4)_3 \cdot 2H_2O$ is 3.88 V vs Li.

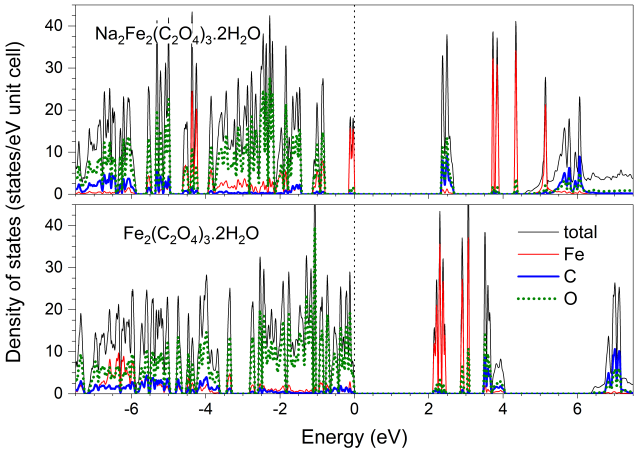

Figure 6. Total and projected electronic density of states of $Na_2Fe_2(C_2O_4)_3 \cdot 2H_2O$ and the (hypothetical) desodiated end compound $Fe_2(C_2O_4)_3 \cdot 2H_2O$. The zero of the energy (at 0 eV) is set to the highest occupied state.

The migration of Na in $Na_2Fe_2(C_2O_4)_3 \cdot 2H_2O$ was studied by considering the movement of a V_{Na}^- vacancy (the void formed by the removal of a Na^+ ion) from one Na lattice site to another or, equivalently, the movement of the Na^+ ion in the opposite direction. **Figure 7** shows two possible migration paths for V_{Na}^-: one is along the **1–2–3** Na zigzag chains (c-axis) and the other involves the **4–1** segment. Using the NEB method, the energy barriers were estimated to be 0.40 eV for the **1-2–3** path and 1.22 eV for the **4–1**

path. The migration of Na in the title compound is thus effectively along the *c*-axis with a migration barrier comparable to those previously calculated for Li migration in olivine-type $LiFePO_4$[39] and $LiMn_2O_4$ spinel.[40] For comparison, Li migration in the Li analog, $Li_2Fe_2(C_2O_4)_3 \cdot 2H_2O$, was studied in the same manner and the barrier was estimated to be 0.41 eV (along **1**–**2**–**3**) or 1.05 eV (along **4**–**1**).

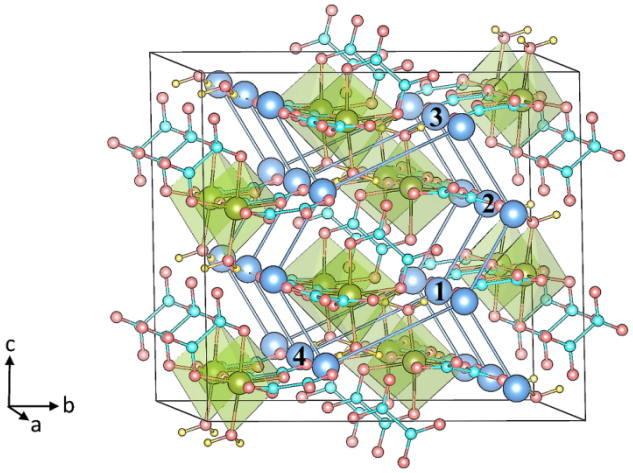

Figure 7. Possible Na migration paths in $Na_2Fe_2(C_2O_4)_3 \cdot 2H_2O$.

We also explored the possibility of forming Fe antisite defects in the material that could, in principle, end up blocking Na migration along the *c*-axis. However, the formation energy of the Fe/Na antisite defect pair, i.e., Fe_{Na}^{+}–Na_{Fe}^{-} (Fe^{2+} at the Na^+ site and Na^+ at the Fe^{2+} site) in $Na_2Fe_2(C_2O_4)_3 \cdot 2H_2O$ was found to be rather high, 1.12 eV, in calculations using 2×1×2 supercells, suggesting that the concentration of the antisite defects could be negligible. For comparison, the formation energy of the Fe/Li antisite pair, i.e., Fe_{Li}^{+}–Li_{Fe}^{-}, in $Li_2Fe_2(C_2O_4)_3 \cdot 2H_2O$ was calculated to be 0.41 eV, even lower than that of the Fe/Li antisite pair in $LiFePO_4$ (0.51 eV).[39] The concentration of the antisites in the Li analog is thus expected to be significant, especially if the material is prepared directly using high-temperature methods. The low energy in the case of Fe/Li can be ascribed to the comparable ionic radii of Li^+ (0.76 Å) and high-spin Fe^{2+} (0.78 Å). It remains to be seen if the antisite defects can also form during cycling in LIBs.

IV. CONCLUSION

In conclusion, an iron-based oxalate compound $Na_2Fe_2(C_2O_4)_3 \cdot 2H_2O$ has been shown to be electrochemically active as a positive electrode material in NIBs. It delivered a stable capacity approaching the theoretical value (117 $mAhg^{-1}$) when cycled in the range 1.7–4.2 V at an applied current of 5 mAg^{-1}. Mössbauer spectroscopy and first-principles calculations confirmed the redox activity of the material, in contrast to the behavior exhibited when cycled in lithium-ion batteries. The title compound exhibits an energy density as high as 326 $Whkg^{-1}$, which is among the best iron-based polyanionic cathodes for NIBs. Therefore, the present study offers a promising cathode material for NIBs which is inherently low-cost and environmentally friendly.

ASSOCIATED CONTENT

Supporting Information. Crystallographic data, Mössbauer analysis, PXRD pattern of ball-milled sample, the first 15 cycles of prepared cell, Nyquist plots of cells at different cycles, and Rietveld refinement of powder XRD on the charged sample are attached as the supporting file. This material is available free of charge via the Internet at http://pubs.acs.org.

AUTHOR INFORMATION

Corresponding Author

*pl@st-andrews.ac.uk (PL); *ara@st-andrews.ac.uk(ARA)

Author Contributions

The manuscript was written through contributions of all authors. All authors have given approval to the final version of the manuscript.

ACKNOWLEDGMENT

We thank Prof. John T. S. Irvine and Dr. Paul Connor (School of Chemistry, University of St Andrews) for electrochemical test support. Thanks to Mr. Pifu Gong and Prof. Zheshuai Lin (Technical Institute of Physics and Chemistry, Chinese Academy of Sciences) for helpful discussions. W. Y. thanks the Royal Society for the award of a Newton International Fellowship (140881). The calculations were carried out using computing resources at the Center for Computationally Assisted Science and Technology at North Dakota State University.

REFERENCES

[1] Larcher, D.; Tarascon, J. M. Towards greener and more sustainable batteries for electrical energy storage. *Nature Chem.* **2015**, *7*, 19–29.

[2] Pan, H. L.; Hu, Y. S.; Chen, L. Q. Room-temperature stationary sodium-ion batteries for large-scale electric energy storage. *Energy Environ. Sci.* **2013**, *6*, 2338–2360.

[3] Yabuuchi, N.; Kubota, K.; Dahbi, M.; Komaba, S. Research development on sodium-ion batteries. *Chem. Rev.* **2014**, *114*, 11636–11682.

[4] Takeda, Y.; Nakahara, K.; Nishijima, M.; Imanishi, N.; Yamamoto, O. Sodium deintercalation from sodium iron oxide. *Mater. Res. Bull.* **1994**, *29* (6), 659–666.

[5] Yabuuchi, N.; Kajiyama, M.; Iwatate, J.; Nishikawa, H.; Hitomi, S.; Okuyama, R.; Usui, R.; Yamada, Y.; Komaba, S.P2-type $Na_x[Fe_{1/2}Mn_{1/2}]O_2$ made from earth-abundant elements for rechargeable Na batteries. *Nature Mater.* **2012**, *11*, 512–517.

[6] Kubota, K.; Yabuuchi, N.; Yoshida, H.; Dahbi, M.; Komaba, S. Layered oxides as positive electrode materials for Na-ion batteries. *MRS Bull.* **2014**, *29*, 416–422

[7] Ellis, B. L.; Makahnouk, W. R. M.; Makimura, Y.; Toghill, K.; Nazar, L. F. A multifunctional 3.5 V iron-based phosphate cathode for rechargeable batteries. *Nature Mater.* **2007**, *6*, 749–755.

[8] Ellis, B. L.; Makahnouk, W. R. M.; Weetaluktuk, W. N. R.; Ryan, D. H.; Nazar, L. F. Crystal structure and electrochemical properties of A_2MPO_4F fluorophosphates (A = Na, Li; M = Fe, Mn, Co, Ni). *Chem. Meter.* **2010**, *22*, 1059–1070.

[9] Moreau, P.; Guyomard, D.; Gaubicher, J.; Boucher, F. Structure and stability of sodium intercalated phases in olivine $FePO_4$. *Chem. Mater.* **2010**, *22* (14), 4126–4128.

[10] Barpanda, P.; Ye, T.; Nishimura, S.; Chung, S. C.; Yamada, Y.; Okubo, M.; Zhou, H.; Yamada. A. Sodium iron pyrophos-

phate: A novel 3.0 V iron-based cathode for sodium-ion batteries. *Electrochem. Commu.* **2012**, *24*, 116–119.

[11] Kim, H.; Park, I.; Seo, D. H.; Lee, S.; Kim, S. W.; Kwon, W. J.; Park, Y. U.; Kim, C. S.; Jeon, S.; Kang, K. New iron-based mixed-polyanion cathodes for lithium and sodium rechargeable batteries: combined first principles calculations and experimental study. *J. Am. Chem. Soc.* **2012**, *134*, 10369–10372.

[12] Munaò, I.; Zvereva, A. E.; Volkova, S. O.; Vasiliev, A.; Armstrong, R.; Lightfoot; P. $NaFe_3(HPO_3)_2((H,F)PO_2OH)_6$: A Potential Cathode Material and a Novel Ferrimagnet. *Inorg. Chem.* **2016**, *55* (5), pp 2558–2564.

[13] Gond, R.; Meena, S.; Yusuf, S. M.; Shukla, V.; Jena, K. N.; Ahuja, R.; Okada, S.; Barpanda, P. Enabling the Electrochemical Activity in Sodium Iron Metaphosphate $[NaFe(PO_3)_3]$ Sodium Battery Insertion Material: Structural and Electrochemical Insights. *Inorg. Chem.* **2017**, 56 (10), 5918-5929.

[14] Barpanda, P.; Oyama G.; Nishimura, S.; Chung S. C.; Yamada, A. A 3.8-V earth-abundant sodium battery electrode. *Nat. Commu.* **2014**, *5*, 4358–4365.

[15] Banerjee, A.; Araujo, B. R.; Ahuja; R. Unveiling the thermodynamic and kinetic properties of $Na_xFe(SO_4)_2$ (x = 0–2): toward a high capacity and low-cost cathode material. *J. Mater. Chem. A*, **2016**, *4*, 17960–17969.

[16] Yao, W.; Sougrati, M.-T.; Hoang, K.; Hui, J.; Lightfoot, P.; Armstrong, A. R. $Na_2Fe(C_2O_4)F_2$: a new iron-based polyoxyanion cathode for Li/Na ion batteries. *Chem. Mater.*, **2017**, 29(5), 2167–2172.

[17] Ahouari, H.; Rousse, G.; Carvajal, J. R.; Sougrati, M. T.; Saubanère, M.; Courty, M.; Recham, N.; Tarascon, J. M. Unraveling the structure of iron(III) oxalate tetrahydrate and its reversible Li insertion capability. *Chem. Mater.* **2015**, *27*, 1631–1639.

[18] Wang, X. F.; Kurono, R.; Nishimura, S.; Okubo, M.; Yamada, A. Iron–oxalato framework with one-dimensional open channels for electrochemical sodium-ion intercalation. *Chem. Eur. J.* **2015**, *21*, 1096–1101.

[19] Ahouari, H.; Rousse, G.; Klein, Y.; Chotard, J. N.; Sougrati, M. T.; Recham, N.; Tarascon, J. M. Synthesis, structure & electrochemical properties of metal malonate $Na_2M(H_2C_3O_4)_2 \cdot nH_2O$ (n=0, 2) compounds and comparison with oxalate $Na_2M_2(C_2O_4)_3 \cdot 2H_2O$ compounds. *Solid State Sci.* **2015**, *42*, 6–13.

[20] Yamaguchi, H.; Kimura, S.; Honda, Z.; Okunishi, K.; Todo, S.; Kindo, K.; Hagiwara, M. High-Field Magnetism of the Spin-Ladder Material $Na_2Fe_2(C_2O_4)_3(H2O)_2$. *J. Phys. Soc. Jpn.* **2009**, *78*(12), 124701.

[21] Kikkawa, A.; Katsumata, K.; Honda, Z.; Yamada K. The Magnetic Property of a Uniaxial Spin–Ladder Material $Na_2Fe_2(C_2O_4)_3(H_2O)_2$. *J. Phys. Soc. Jpn.* **2005**, *74*, 2687.

[22] Perdew, J. P.; Burke, K.; Ernzerhof, M. Generalized gradient approximation made simple. *Phys. Rev. Lett.* **1996**, *77*, 3865–3858.

[23] Blochl, P. E. Projector augmented-wave method. *Phys. Rev. B* **1994**, *50*, 17953–17979.

[24] Kresse, G.; Furthmüller, J. Efficiency of ab-initio total energy calculations for metals and semiconductors using a plane-wave basis set. *Comput. Mat. Sci.* **1996**, *6*, 15–50.

[25] Dudarev, S. L.; Botton, G. A.; Savrasov, S. Y.; Humphreys, C. J.; Sutton, A. P. Electron-energy-loss spectra and the structural stability of nickel oxide: An LSDA+U study. *Phys. Rev. B* **1998**, *57*, 1505–1509.

[26] Grimme, S. Semiempirical GGA-type density functional constructed with a long-range dispersion correction. *J. Comp. Chem*. **2006**, *27*, 1787–1799.

[27] Henkelman, G.; Uberuaga, B. P.; Jónsson, H. A Climbing Image Nudged Elastic Band Method for Finding Saddle Points and Minimum Energy Paths. *J. Chem. Phys.* **2000**, *113* (22), 9901–9904.

[28] Wei, A. A.; Yan, L. C.; Chui, L. W.; Raghavan, P.; Huey, H. H.; Srinivasan, M. Mesoporous Cobalt Oxalate Nanostructures as High-Performance Anode Materials for Lithium-Ion Batteries: Ex Situ Electrochemical Mechanistic Study. *J. Phys. Chem. C* **2013**, *117*, 16316–16325.

[29] Wu, X.; Guo, J.; McDonald, M.- J.; Li, S.; Xu, B.; Yang, Y. Synthesis and characterization of urchin-like $Mn_{0.33}Co_{0.67}C_2O_4$ for Li-ion batteries: Role of SEI layers for enhanced electrochemical properties. *Electrochimica Acta* **2015**, *163*, 93–101.

[30] Strobridge, F. C.; Clement, R. J; Leskes, M.; Middlemiss, D. S.; Borkiewicz, O. J.; Wiaderek, K. M.; Chapman, K. W.; Chupas, P. J.; Grey C. P. Identifying the Structure of the Intermediate, $Li_{2/3}CoPO4$, Formed during Electrochemical Cycling of $LiCoPO4$. *Chem. Mater.* **2014**, *26*, 6193-6205.

[31] Bianchini, M.; Fauth, F.; Suard, E.; Leriche, J. B.; Masquelier, C.; Croguennec, L. Spinel materials for Li-ion batteries: New insights obtained by operando neutron and synchrotron X-ray diffraction. *Acta Cryst.* **2015**, *B71*, 688-701.

[32] Armstrong, R.; Dupre, N.; Paterson, A. J.; Grey, C. P.; Bruce, P. G. Combined Neutron Diffraction, NMR, and Electrochemical Investigation of the Layered-to-Spinel Transformation in $LiMnO_2$. *Chem. Mater.* **2004**, *16*, 3106–3118.

[33] Kojima, A.; Kojima, T.; Sakai, T. Structural Analysis during Charge-Discharge Process of Li_2FeSiO_4 Synthesized by Molten Carbonate Flux Method. *J. Electrochem. Soc.* **2012**, *159* (5), A525–A531.

[34] Lv, D.; Bai, J.; Zhang, P.; Wu, S.; Li, Y.; Wen, W.; Jiang, Z.; Mi, J.; Zhu, Z.; Yang, Y. Understanding the High Capacity of Li2FeSiO4: In Situ XRD/XANES Study Combined with First-Principles Calculations. *Chem. Mater.* **2013**, *25*, 2014–2020.

[35] Nishimura, S.; Nakamura, M.; Natsui, R.; Yamada, A. New Lithium Iron Pyrophosphate as 3.5 V Class Cathode Material for Lithium Ion Battery. *J. Am. Chem. Soc.* **2010**, *132*, 13596–13597.

[36] Kim, H.; Lee, S.; Park, Y.; Kim, H.; Kim, J.; Jeon, S.; Kang, K. Neutron and X-ray Diffraction Study of Pyrophosphate-Based $Li_{2-x}MP_2O_7$ (M = Fe, Co) for Lithium Rechargeable Battery Electrodes. *Chem. Mater.* **2011,** *23*, 3930–3937.

[37] Oyama, G.; Pecher, O.; Griffith, K. J.; Nishimura, S. Pigliapochi, R. Grey, C. P.; Yamada, A. Sodium Intercalation Mechanism of 3.8 V Class Alluaudite Sodium Iron Sulfate, *Chem. Mater.* **2016**, 28, 5321–5328.

[38] Hoang, K. Defect Physics, Delithiation Mechanism, and Electronic and Ionic Conduction in Layered Lithium Manganese Oxide Cathode Materials, *Phys. Rev. Applied* **2015**, *3*, 024013.

[39] Hoang, K.; Johannes, M. Tailoring Native Defects in $LiFePO_4$: Insights from First-Principles Calculations, *Chem. Mater.* **2011**, *23*, 3003–3013.

[40] Hoang, K. Understanding the electronic and ionic conduction and lithium over-stoichiometry in $LiMn_2O_4$ spinel, *J. Mater. Chem. A* **2014**, *2*, 18271–18280.

Table of Contents (TOC)